Research Article

Multi-field Semi-Lagrangian Reproducing Kernel Particle Method for Landslide Simulation

Thanakorn Siriaksorn[1] and Sheng-Wei Chi[2*]

[1]Ph.D. Candidate, Department of Civil and Materials Engineering, University of Illinois at Chicago, Chicago, IL 60607

[2]Assistant Professor, Department of Civil and Materials Engineering, University of Illinois at Chicago, Chicago, IL 60607

Abstract

This paper presents a multi-field meshfree method based on a semi-Lagrangian reproducing kernel particle method for simulation of landslide processes. In the proposed method, the approximation functions of field variables are constructed based on particles, without the need of grids or structured mesh, and the discrete state variables follow the particles, thus Lagrangian description; while the interpolation function of each particle is continually updated during deformation. The formulation naturally handles extremely large deformation and material separation, thus the method is well-suited to capture the deformation of geomaterials transitioning from elastic to an almost fluid-like deformation mode during a landslide event. The general Biot theory is incorporated in the multi-field semi-Lagrangian formulation to describe the behaviors of porous geomaterials. Several numerical examples are presented for verification of the proposed method and a landslide simulation is validated against experimental results.

Introduction

Landslide is one of the most destructive natural disasters. According to the study in [1] and [2], the deadliest landslide in the 20th century happened in Haiyuan, China, 1920; the incident was estimated to have fatalities of more than 100,000. Further, the impacts of landslides on properties or economics can also be crucial. For instance, Thistle landslide in Utah, 1983, costs more than US$600 million (based on U.S. dollars in 1983) [3,4].

Many attempts have been made to model landslide activities for many decades in order to predict and, ultimately, mitigate the impacts of landslides. However, full analysis of landslide hazards, which involve complex poromechanics, transition of material behaviors from solid-like to fluid-like, extremely large deformations, material separations, etc., poses difficulties in numerical analyses. To circumvent the numerical difficulties, a full landslide process is typically broken down into three stages: pre-failure, failure, and post-failure, for each of which different numerical analysis or modeling techniques are adopted separately [5]. The analyses for these stages are usually regarded as slope stability analysis and run-out analysis[5].

Slope stability is commonly analyzed by the Limit Equilibrium Methods (LEMs) and Finite Element Methods (FEMs). LEMs were developed to analyze stability of embankments [6-8] and slopes [9-13] by considering certain equilibrium conditions of a pre-defined slip surface to determine the factor of safety, which is taken as an indicator for the stability of a slope. On the other hand, FEM, a powerful tool for solutions of partial differential equations, can be used to determine local strain/deformation of a slope. A few of many applications of FEM on slope stability analysis can be found in [14-16].

Popularly used numerical methods for the run-out analysis are the Smoothed Particle Hydrodynamics (SPH) and Discrete Element Method (DEM). SPH [17,18] uses kernel functions as the approximation functions for the solutions of the problems. However, it suffers from boundary deficiency and tensile instability due to the inconsistency of the kernel approximation [19-21]. Some examples of run-out simulations using SPH are [22-27]. DEM is a particle-based method, which uses an explicit temporal discretization scheme to determine the positions of particles, then calculates the interaction forces between the contacting elements, and obtains the velocity of each discrete element from the equation of motion [28]. There are also many DEM applications on simulations of landslide run-out, to name a few, [29-32]. Nonetheless, the simple element-to-element contact models that are typically used in DEM have to be carefully calibrated to the bulk material properties, and it is unclear that these models can be extrapolated to accurately capture landslide phenomena.

To combine capabilities and advantages of continuum-based method with discontinuum-based method, a combined finite/discrete element method [33] was employed to model the entire landslide

processes (i.e., from initiation stage to deposition stage) [34,35]. The landscape is first modeled by FEM, in which a solid constitutive model is incorporated. When certain strain criteria are satisfied in a local region and material damage starts to form and progress, DEM is taken to model such damaged region, solely accounting for the interaction between contacting elements. However, the combined method is difficult to verify mathematically due to the inconsistency between the two numerical techniques.

To overcome the aforementioned numerical issues within one mathematical framework, this paper presents the semi-Lagrangian Reproducing Kernel Particle Method (RKPM) for landslide simulations. The method is extended from the RKPM [36,37], in which the approximation function is constructed purely based on points and can meet desired order of consistency and smoothness; hence, it can analyze slope stability as effective as FEM, while higher order solution accuracy can be readily achieved by increasing the order of consistency. The semi-Lagragian RKPM is well-suited for extremely large deformation analysis since the approximation function is constructed in the current configuration [38,39], which naturally allows for material separation and avoids breaking down in the deformation mapping. The contact between damaged materials in the semi-Lagrangian formulation can be modeled by employing the contact detection algorithm in [40] with further enhanced accuracy using a level-set algorithm [41]. In addition, in order to adequately represent poromechanics of geomaterial, the saturated two-phase deforming porous media model following Biot theory [42-44] is incorporated into the framework.

The remainders of the paper are as follows: Mechanics of porous media is described in Section 2. Semi-Lagrangian RKPM for poromechanics is presented in Section 3. Stabilized nodal integration methods are reviewed in Section 4. In Section 5, the governing equations described in Section 2 are solved under the semi-Lagrangian RKPM framework. In Section 6, several numerical examples to verify the method including landslide simulations are shown. The concluding remarks are given in Section 7.

Deformable Porous Mechanics

The interaction between the interfaces of solid and fluid phases constitutes unique porous mechanical behaviors in granular materials. To account for the coupling effect between phases based on the hypothesis of continuum mechanics, the saturated multiphase formulation, extended from Biot theory [44], is employed. In this paper, a two-field formulation considering the solid displacement and pore water pressure is adopted and described in the following sections.

Governing Equations

Under the assumptions of no phase change and isothermal condition, the governing equations, which consist of the balance of momentum equation and continuity equation, can be respectively expressed by

$$\sigma_{ij,j} + b_i = \rho \ddot{u}_i \quad \text{in} \quad \Omega \tag{1}$$

$$\alpha \dot{u}_{i,i} + \frac{\dot{P}}{M} + q_{i,i} = 0 \quad \text{in} \quad \Omega \tag{2}$$

where σ_{ij} is the total stress, b_i is the body force, ρ is the total density

of porous medium, u_i is the displacement of solid skeleton, Ω is the problem domain, α is the Biot coefficient, P is the pore water pressure, and q_i is the superficial velocity of water flow. M is regarded as Biot compressibility modulus and can be defined by

$$\frac{1}{M} = \frac{\alpha - n}{K_s} + \frac{n}{K_w} \tag{3}$$

where n is the porosity, K_s is the bulk modulus of solid grains, and K_w is the bulk modulus of water.

The total density of porous medium ρ is described as

$$\rho = (1-n)\rho_s + n\rho_w \tag{4}$$

where ρ_s and ρ_w are the density of solid skeleton and water, respectively. The porosity n is the ratio between the void volume V^v and total volume V, that is

$$n = \frac{V^v}{V} \tag{5}$$

By introducing the Biotcoefficient α, the total stress σ_{ij} can be decomposed as

$$\sigma_{ij} = \bar{\sigma}_{ij} - \alpha P \delta_{ij} \tag{6}$$

where $\bar{\sigma}_{ij}$ is the effective stress of solid phase, and δ_{ij} is the second-order identity tensor. Since $\bar{\sigma}_{ij}$ is fully decomposed from the fluid phase, it can be computed using constitutive models of solid, for instance, elasticity or plasticity models. The Biot coefficient α serves as a means of effective stress reduction in porous media and can be interpolated by

$$\alpha = 1 - \frac{K}{K_s} \tag{7}$$

where K is the bulk modulus of porous medium.

For isotropic porous media, the relationship between the flux or superficial velocity of water q_i and pore water pressure P can be described by using Darcy's law

$$q_i = -\frac{k_w}{\mu_w}\left(P_{,i} - \rho_w g_i\right) \tag{8}$$

where k_w is the intrinsic permeability, μ_w is the dynamic viscosity of water, and g_i is the gravity.

The corresponding boundary and initial conditions of the governing equations (1) and (2) are defined as

$$\sigma_{ij} n_j = h_i \quad \text{on} \quad \Gamma_h \tag{9}$$

$$u_i = u_i^g \quad \text{on} \quad \Gamma_g \tag{10}$$

$$-q_i n_i^w = v_s^w \quad \text{on} \quad \Gamma_s \tag{11}$$

$$P = P_r \quad \text{on} \quad \Gamma_r \tag{12}$$

$$u_i(\mathbf{x},t)\big|_{t=0} = u_i^0(\mathbf{x}) \quad \text{in} \quad \Omega \tag{13}$$

$$\dot{u}_i(\mathbf{x},t)\big|_{t=0} = \dot{u}_i^0(\mathbf{x}) \quad \text{in} \quad \Omega \tag{14}$$

$$P(\mathbf{x},t)|_{t=0}= P_0(\mathbf{x}) \quad \text{in} \quad \Omega \tag{15}$$

where n_j and n_i^w are unit normal vectors in the outward direction of corresponding boundaries Γ_h and Γ_r. h_i is the prescribed traction. u_i^g is the prescribed displacement. v_s^w is the prescribed water inflow. P_r is the prescribed pore water pressure. Γ_h and Γ_s are Neumann and Dirichlet boundaries associated with porous medium in the current configuration, respectively. Γ_c and Γ_r are Neumann and Dirichlet boundaries associated with water in the current configuration, respectively. $u_i^0(\mathbf{x})$ is the initial value of displacement of the porous medium. $\dot{u}_i^0(\mathbf{x})$ is the initial value of velocity of the porous medium. $P_0(\mathbf{x})$ is the initial value of pore water pressure.

Constitutive Equations

The Drucker-Prager plasticity model with associated flow rule in conjunction with a damage model [45-47] is adopted to represent geomaterial behaviors from material yielding to material separation. The yield function of Drucker-Prager can be defined as

$$f = \sqrt{2J_2} + BI_1 - k \tag{16}$$

where I_1 is the first invariant of $\hat{\sigma}_{ij}$. J_2 is the second invariant of the deviatoric part of $\hat{\sigma}_{ij}$. B and k are material constants. $\hat{\sigma}_{ij}$ is the effective stress before taking into account material damage, that is

$$\hat{\sigma}_{ij} = \frac{\bar{\sigma}_{ij}}{(1-d)} \tag{17}$$

where d is the damage parameter defined by

$$d = c_1(\eta - c_2)\big/\big(\eta(c_1 - c_2)\big) \quad ; \quad \eta > c_2 \tag{18}$$

c_1 and c_2 are material constants specifying critical point (when damage reaches maximum, for instance, $d=1$) and initiation point (when material starts to damage), respectively. η is the norm of the strain tensor (i.e., $\eta = \sqrt{\varepsilon_{ij}\varepsilon_{ji}}$). In this study, d is limited to be slightly less than 1 to sustain some compressive strength of the material after it is fully damaged.

The material parameters B and k of Drucker-Prager can be related to the cohesion c and friction angle ϕ of Mohr-Coulomb as

$$B = \frac{2\sqrt{6}\sin\phi}{3(3-\sin\phi)} \tag{19}$$

$$k = \frac{2\sqrt{6}c\cos\phi}{3-\sin\phi} \tag{20}$$

To take into account large deformation, the numerical integration of incremental constitutive equation is carried out by employing the approach proposed in [48]

$$\bar{\sigma}_{ij}^{n+1} = T_{ik}^{n+1}\bar{\sigma}_{kl}^n T_{lj}^{n+1} + \tilde{C}_{ijkl}\Delta\varepsilon_{kl}^{n+0.5} \tag{21}$$

where $\tilde{C}_{ijkl}$ is elasto-plastic-damage material tangent tensor. T_{ik}^{n+1}, T_{lj}^{n+1} are the transformation matrices denoted by

$$T_{ij}^{n+1} = \delta_{ij} + \left(\delta_{ik} - \frac{1}{2}w_{ik}^{n+0.5}\right)^{-1} w_{kj}^{n+0.5} \tag{22}$$

with $\quad w_{ij}^{n+0.5} = \Delta u_{[i,j]}^{n+0.5} = \frac{1}{2}\left(\frac{\partial\Delta u_i}{\partial x_j^{n+0.5}} - \frac{\partial\Delta u_j}{\partial x_i^{n+0.5}}\right) \tag{23}$

The incremental strain $\Delta\varepsilon_{kl}^{n+0.5}$ is expressed as

$$\Delta\varepsilon_{kl}^{n+0.5} = \Delta u_{(i,j)}^{n+0.5} = \frac{1}{2}\left(\frac{\partial\Delta u_i}{\partial x_j^{n+0.5}} + \frac{\partial\Delta u_j}{\partial x_i^{n+0.5}}\right) \tag{24}$$

with $\quad \dfrac{\partial\Delta u_i}{\partial x_j^{n+0.5}} = \dfrac{\partial\Delta u_i}{\partial x_k}\dfrac{\partial x_k}{\partial x_j^{n+0.5}} \tag{25}$

The superscript $n+0.5$ denotes that the corresponding variables are evaluated from the configuration at time step $n+0.5$ [48].

Semi-Lagrangian RKPM

In the Lagrangian RKPM, mapping between current configuration and initial configuration is required, i.e., $\mathbf{x} = \varphi(\mathbf{X},t)$. Here X refers to the Lagrangian coordinates, x refers to the Eulerian coordinates, and φ is the mapping function. This mapping between the two configurations may break down when extreme deformation occurs. To circumvent such issue, the shape functions of semi-Lagrangian RKPM is constructed in the current configuration, thus eliminating the necessity of mapping. The discretization (i.e., nodal points) of semi-Lagrangian RKPM is however still under Lagrangian description to track internal variables of the same material points at each time step. These properties of semi-Lagrangian RKPM, illustrated in Figure 1, are advantageous for problems involving extremely large deformation and material separation [39,42].

The shape function of semi-Lagrangian RKPM is expressed as

$$\Psi_I(\mathbf{x}) = C(\mathbf{x};\mathbf{x}-\mathbf{x}_I)\Phi_a(\mathbf{x}-\mathbf{x}_I) \tag{26}$$

where $\Psi_I(\mathbf{x})$ is the shape function of node I constructed in the current configuration and $\mathbf{x}_I = \mathbf{x}(\mathbf{X}_I,t)$ is the nodal position of node I in the current configuration. The correction function $C(\mathbf{x};\mathbf{x}-\mathbf{x}_I)$ $\Phi_a(\mathbf{x}-\mathbf{x}_I)$ and the kernel function are also determined in the current configuration. The kernel function controls the smoothness and locality of the approximation function, and hence it should be selected depending on the characteristics of the problem, e.g., the order of Partial Differential Equations (PDEs). The 3-D kernel function is constructed by the product of 1-D kernel function

$$\Phi_a(\mathbf{x}-\mathbf{x}_I) = \prod_{i=1}^{3}\Phi_a^{1\text{-}D}(z_i) \tag{27}$$

with $\quad z_i = \dfrac{|x_i - x_i(\mathbf{X}_I,t)|}{a_i} \tag{28}$

Subscript a in the kernel function is a number defining the influence domain or so-called support size of the function. This
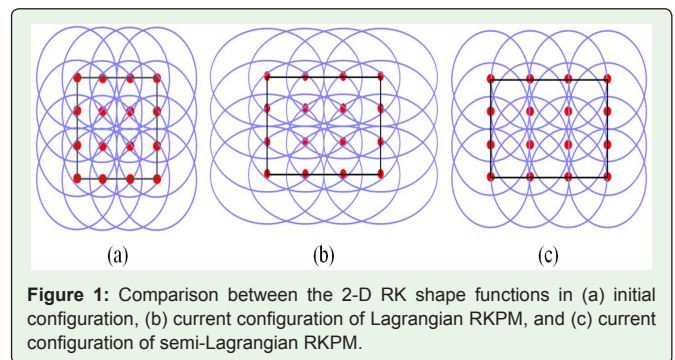

Figure 1: Comparison between the 2-D RK shape functions in (a) initial configuration, (b) current configuration of Lagrangian RKPM, and (c) current configuration of semi-Lagrangian RKPM.

Citation: Siriaksorn T and Chi S. Multi-field Semi-Lagrangian Reproducing Kernel Particle Method for Landslide Simulation. SM J Biomed Eng. 2017; 3(2): 1014s.

Page 3/10

value is usually regarded after normalized by nodal distance. In this work, a cubic spline function, which is of class C^2, is employed as the kernel function and a normalized support size of 1.5 is used, unless otherwise mentioned.

The correction function is introduced to enforce the reproducing conditions to achieve reproducibility for monomials up to the specified n^{th} order consistency, that is

$$C\left(\mathbf{x};\mathbf{x}-\mathbf{x}_I\right) = \sum_{|\alpha|=0}^{n} \left(\mathbf{x}-\mathbf{x}_I\right)^{\alpha} b_{\alpha}(\mathbf{x}) \qquad (29)$$

where $\alpha = (\alpha_1, \alpha_2, \ldots, \alpha_m)$ denotes the m-dimensional index, with its length defined as $|\alpha| \equiv \sum_{i=1}^{m} \alpha_i$; $(\mathbf{x}-\mathbf{x}_I)^{\alpha} \equiv (x_1 - x_{1I})^{\alpha_1}(x_2 - x_{2I})^{\alpha_2}\cdots(x_m - x_{mI})^{\alpha_m}$; $b_{\alpha} \equiv b_{\alpha_1, \alpha_2, \ldots, \alpha_m}$; $b_{\alpha}(\mathbf{x})$ are the corresponding coefficient of the monomials $(\mathbf{x}-\mathbf{x}_I)^{\alpha}$.

The coefficients b(x) are obtained by satisfying the nth order reproducing condition

$$\sum_{I=1}^{NP} \Psi_I(\mathbf{x})\mathbf{x}_I^{\alpha} = \mathbf{x}^{\alpha} \qquad ; \qquad |\alpha| \le n \qquad (30)$$

where *NP* is the total number of nodes. Linear basis (i.e., n=1) is used in this paper. By using equations (26) and (29) and imposing the reproducing condition in (30), the corresponding coefficients b(x) can be determined as

$$\mathbf{b}(\mathbf{x}) = \mathbf{M}^{-1}(\mathbf{x})\mathbf{H}(\mathbf{0}) \qquad (31)$$

where M(x) is the moment matrix described as

$$\mathbf{M}(\mathbf{x}) = \sum_{I=1}^{NP} \mathbf{H}\left(\mathbf{x}-\mathbf{x}_I\right)\mathbf{H}^T\left(\mathbf{x}-\mathbf{x}_I\right)\Phi_a\left(\mathbf{x}-\mathbf{x}_I\right) \qquad (32)$$

and H(x-x$_I$) is the vector of monomial basis functions.

Substituting equation (31) into equations (29) and (26), the shape function reads

$$\Psi_I(\mathbf{x}) = \mathbf{H}^T(\mathbf{0})\mathbf{M}^{-1}(\mathbf{x})\mathbf{H}\left(\mathbf{x}-\mathbf{x}_I\right)\Phi_a\left(\mathbf{x}-\mathbf{x}_I\right) \qquad (33)$$

In the semi-Lagrangian RKPM, the approximation of velocity v_i is defined as

$$\dot{u}_i^h(\mathbf{x},t) = v_i^h(\mathbf{x},t) = \sum_{I=1}^{NP} \Psi_I(\mathbf{x})v_{iI}(t) \qquad (34)$$

where $v_{iI}(t)$ is the nodal coefficient of velocity. Taking temporal derivative of equation (34), the approximation of the acceleration a_i is expressed as

$$\ddot{u}_i^h(\mathbf{x},t) = a_i^h(\mathbf{x},t) = \sum_{I=1}^{NP} \left(\Psi_I(\mathbf{x})a_{iI}(t) + \overline{\Psi}_I(\mathbf{x})v_{iI}(t)\right) \qquad (35)$$

where $a_{iI}(t)$ is the nodal coefficient of acceleration. $\overline{\Psi}_I(\mathbf{x})$ is the change of the RK shape function with respect to time, due to the reconstruction of the shape function in semi-Lagrangian RKPM. This term is interpreted as a convection term to carry the information history during the transition between the old shape function and the new one. It is defined as

$$\overline{\Psi}_I(\mathbf{x}) = C\left(\mathbf{x};\mathbf{x}-\mathbf{x}_I\right)\dot{\Phi}_a\left(\mathbf{x}-\mathbf{x}_I\right) \qquad (36)$$

The temporal derivative of the correction function is omitted since the function is constructed by solving the corresponding coefficient b(x) under the current configuration [39,42]. By considering equations (27) and performing the chain rule, the temporal derivative of the kernel function $\dot{\Phi}_a\left(\mathbf{x}-\mathbf{x}(\mathbf{X}_I,t)\right)$ is obtained as

$$\dot{\Phi}_a(\mathbf{x}-\mathbf{x}_I) = \prod_{i=1}^{3}\left(\frac{1}{a_i}\cdot\frac{\partial\Phi_a^{1D}(z_i)}{\partial(z_i)}\cdot\frac{x_i - x_i(\mathbf{X}_I,t)}{|x_i - x_i(\mathbf{X}_I,t)|}\cdot\frac{\partial(x_i - x_i(\mathbf{X}_I,t))}{\partial t}\right) \qquad (37)$$

Stabilized Nodal Integration Methods

Domain integration is required when solving problems by Galerkin formulation. In FEM, this integration is usually carried out by Gauss integration because mapping to parental coordinates is easy with the presence of mesh. For meshfree methods such as RKPM, nodal integration is preferable to preserve the mesh-free property. The advantages of nodal integration are that it is computationally cheaper than Gauss integration and the internal variables are stored at nodes, which is beneficial for large deformation problems.

For demonstration purposes, consider the following equilibrium equation of an elasticity problem

$$\sigma_{ij,j} + b_i = 0 \qquad \text{in} \quad \Omega \qquad (38)$$

$$\sigma_{ij}n_j = h_i \qquad \text{on} \quad \Gamma_h \qquad (39)$$

$$u_i = u_i^g \qquad \text{on} \quad \Gamma_g \qquad (40)$$

where σ_{ij} is the Cauchy stress, b_i is the body force, n_j is the unit normal vector in the outward direction of the Neumann boundaries Γ_h, h_i is the prescribed traction, u_i^g and is the prescribed displacement on the Dirichlet boundaries Γ_g. The Galerkin formulation is described as

$$\int_{\Omega} \delta u_{i,j}^h \sigma_{ij}^h d\Omega = \int_{\Gamma_h} \delta u_i^h h_i d\Gamma + \int_{\Omega} \delta u_i^h b_i d\Omega \qquad (41)$$

For Direct Nodal Integration (DNI), the locations of the integration points are taken at the same positions as nodal points, this causes rank deficiency and instability due to under-integration [49,50]. It also does not satisfy linear exactness and has suboptimal convergence, and hence the Stabilized Conforming Nodal Integration (SCNI) was proposed in [51,52] to remedy such issues. SCNI introduced the assumed strain $\overline{\varepsilon}_{ij}^h$ to avoid the rank deficiency of the stiffness matrix. The assumed strain in SCNI is the averaged strain over a conforming nodal representative domain, which is usually constructed by using Voronoi diagram (Figure 2a). The assumed strain $\overline{\varepsilon}_{ij}^h$ can be expressed as

$$\overline{\mathbf{a}}^h(\mathbf{x}_L) = \sum_{I=1}^{NP} \overline{\mathbf{B}}_I(\mathbf{x}_L)\mathbf{d}_I \qquad (42)$$

where

$$\overline{\mathbf{B}}_I^T(\mathbf{x}_L) = \begin{bmatrix} \overline{b}_{I1}(\mathbf{x}_L) & 0 & 0 & 0 & \overline{b}_{I3}(\mathbf{x}_L) & \overline{b}_{I2}(\mathbf{x}_L) \\ 0 & \overline{b}_{I2}(\mathbf{x}_L) & 0 & \overline{b}_{I3}(\mathbf{x}_L) & 0 & \overline{b}_{I1}(\mathbf{x}_L) \\ 0 & 0 & \overline{b}_{I3}(\mathbf{x}_L) & \overline{b}_{I2}(\mathbf{x}_L) & \overline{b}_{I1}(\mathbf{x}_L) & 0 \end{bmatrix} \qquad (43)$$

with $\overline{b}_{Ii}(\mathbf{x}_L) = \frac{1}{V_L}\int_{\Gamma_L} \Psi_I(\mathbf{x})n_i(\mathbf{x})d\Gamma \qquad (44)$
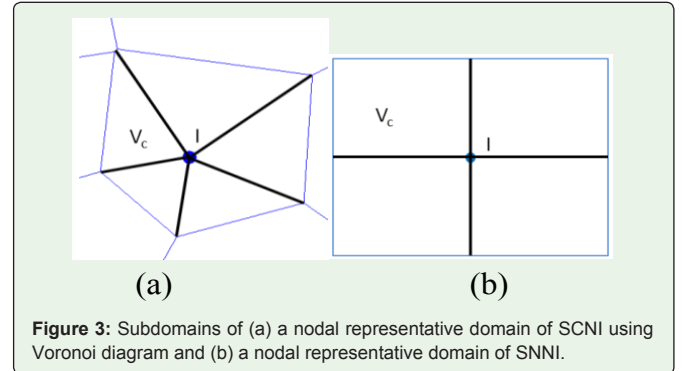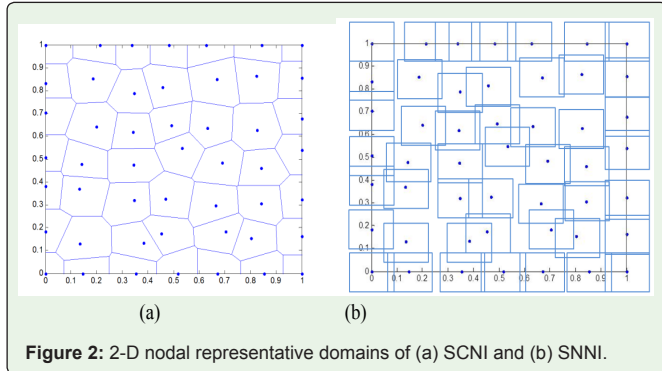
and V_L and Γ_L are the volume and boundary, respectively, of the nodal representative domain of node *L*. d_I is the vector of corresponding nodal coefficient of displacement or so-called generalized displacement.

The method satisfies integration constraints and results in achievement of the first order accuracy of solutions. The integration constraints are described as

$$\sum_L \overline{b}_{Ii}(\mathbf{x}_L)V_L = 0 \quad \text{for} \ \{I : \text{supp}(\Psi_I) \cap \Gamma = \varnothing\} \qquad (45)$$

$$\sum_L \overline{b}_{Ii}(\mathbf{x}_L)V_L = \int_{\Gamma_h} \Psi_I(\mathbf{x})n_i(\mathbf{x})d\Gamma \ \text{for} \ \{I : \text{supp}(\Psi_I) \cap \Gamma_h \ne \varnothing\} \qquad (46)$$

Nevertheless, the requirement of conforming nodal representative domains in SCNI is problematic when encountering large deformation, fracture, separation, or penetration problems. The Stabilized Non-conforming Nodal Integration (SNNI) was proposed by [53] to handle such problems by allowing nodal representative domain to be pre-defined and independent of nodal distribution, thus eliminating the conforming restriction, as can be seen in Figure 2.

Figure 2: 2-D nodal representative domains of (a) SCNI and (b) SNNI.

Figure 3: Subdomains of (a) a nodal representative domain of SCNI using Voronoi diagram and (b) a nodal representative domain of SNNI.

Despite the stabilization in SNNI and SCNI, low energy modes may still be triggered in transient problems and cause instability; this calls for an additional stabilization [54,55]. The Modified Stabilized Conforming Nodal Integration (MSCNI) and Modified Stabilized Non-conforming Nodal Integration (MSNNI) offer a penalty-type stabilization term, which is constructed based on subdomains of each nodal representative domain, as shown in Figure 3.

The discrete form of the internal energy of (41), after including the additional stabilization term is given as

$$\sum_{I=1}^{NP}\left[\overline{\varepsilon}_I(\delta u_i^h)C_{ijkl}\overline{\varepsilon}_I(u_k^h)V_I+\tilde{\alpha}\sum_{c=1}^{Ns_I}\left(\left(\overline{\varepsilon}_I(\delta u_i^h)-\overline{\varepsilon}_c(\delta u_i^h)\right)C_{ijkl}\left(\overline{\varepsilon}_I(u_k^h)-\overline{\varepsilon}_c(u_k^h)\right)V_c\right)\right]\ (47)$$

Where $\underline{C}_{ijkl}$ is elastic material tangent tensor. V_I and V_c are nodal volumes of node I and subdomain c, respectively. Ns_I is the number of subdomains in the nodal representative domain of node I. $\overline{\varepsilon}_I(u_i^h)$ and $\overline{\varepsilon}_c(u_i^h)$ are the smoothed strains of node I and subdomain c, respectively. $\tilde{\alpha}$ is the stabilization parameter ranging between 0 and 1.

In this work, the MSNNI is employed. For more detailed discussions on domain integration issue in meshfree methods, see [56].

Semi-Lagrangian RKPM for Saturated Deformable Porous Media

Using Galerkin formulation and applying the boundary conditions in (9) - (12), the variational equations of the governing equations (1) and (2) are obtained as

$$\int_\Omega \delta u_{i,j}^h \overline{\sigma}_{ij}^h d\Omega - \int_\Omega \delta u_{i,j}^h \alpha P^h \delta_{ij} d\Omega + \int_\Omega \delta u_i^h \rho \ddot{u}_i^h d\Omega = \int_{\Gamma_h} \delta u_i^h h_i d\Gamma + \int_\Omega \delta u_i^h b_i d\Omega \quad (48)$$

$$\int_\Omega \delta P^h \alpha \dot{u}_{i,i}^h d\Omega + \int_\Omega \delta P^h \frac{\dot{P}^h}{M} d\Omega + \int_\Omega \delta P_{,i}^h \frac{k_w}{\mu_w} P_{,i}^h d\Omega = \int_{\Gamma_s} \delta P^h v_s^w d\Gamma + \int_\Omega \delta P_{,i}^h \frac{k_w}{\mu_w} \rho_w g_i d\Omega \quad (49)$$

The variational equations are then discretized by semi-Lagrangian RKPM in space domain and explicit temporal discretization schemes in time domain. Dirichlet boundary conditions are imposed by the boundary singular kernel method [57].

Spatial Discretization

Using semi-Lagrangian RKPM, the equations (48) and (50) are spatially discretized in the current configuration. The approximations of displacement u_i, pore water pressure P, and its time derivative $\dot{P}$ are defined as

$$u_i^h(\mathbf{x},t)=\sum_{I=1}^{NP}\Psi_I(\mathbf{x})d_{iI}(t) \quad (51)$$

$$P^h(\mathbf{x},t)=\sum_{I=1}^{NP}\Psi_I^w(\mathbf{x})P_I(t) \quad (52)$$

$$\dot{P}^h(\mathbf{x},t)=\sum_{I=1}^{NP}\Psi_I^w(\mathbf{x})\dot{P}_I(t) \quad (53)$$

where $d_{iI}(t)$ and $P_I(t)$ are generalized displacement and pore water pressure, respectively. $\Psi_I(\mathbf{x})$ and $\Psi_I^w(\mathbf{x})$ are the semi-Lagrangian shape functions associated with displacement and pore water pressure. In mixed formulation, the choices of the interpolation order of $\Psi_I(\mathbf{x})$ and $\Psi_I^w(\mathbf{x})$ are critical, as the numerical instability can occur if the inf-sup or Ladyzhenskaya-Babuška-Brezzi (LBB) condition [58-60] is violated. One way to remedy the issue is to use the reduced integration technique as stated in [43]. The nodal integration method employed here (i.e., MSNNI) is similar to the reduced integration method with the additional stabilization for the low energy modes, as described in previous section; hence, the equal-order interpolation for $\Psi_I(\mathbf{x})$ and $\Psi_I^w(\mathbf{x})$ is selected for simplicity and efficiency. The spatial derivatives of equations (51) and (52) with respect to current configuration take the following forms:

$$u_{i,j}^h(\mathbf{x},t)=\sum_{I=1}^{NP}\Psi_{I,j}(\mathbf{x})d_{iI}(t) \quad (54)$$

$$P_{,i}^h(\mathbf{x},t)=\sum_{I=1}^{NP}\Psi_{I,i}^w(\mathbf{x})P_I(t) \quad (55)$$

Applying equations (34), (35), and (51)-(55) in the variational equations (48) and (50), the semi-discrete system of equations read

$$\delta d_{iI}\int_\Omega \Psi_{I,j}\overline{\sigma}_{ij}^h d\Omega - \delta d_{iI}\int_\Omega \Psi_{I,j}\alpha\Psi_J^w\delta_{ij}d\Omega P_{,J} + \delta d_{iI}\int_\Omega \Psi_I\rho\Psi_J d\Omega\, \mathrm{a}_{iJ} + \delta d_{iI}\int_\Omega \Psi_I\rho\overline{\Psi}_J d\Omega\, v_{iJ} = \quad (56)$$
$$\delta d_{iI}\int_{\Gamma_h}\Psi_I h_i d\Gamma + \delta d_{iI}\int_\Omega \Psi_I\rho g_i d\Omega$$

$$\delta P_I\int_\Omega \Psi_I^w\alpha\Psi_{J,i}d\Omega v_{iJ} + \delta P_I\int_\Omega \Psi_I^w\frac{\Psi_J^w}{M}d\Omega\dot{P}_J + \delta P_I\int_\Omega \Psi_{I,j}^w\frac{k_w}{\mu_w}\Psi_{J,j}^w d\Omega P_J = \quad (57)$$
$$\delta P_I\int_{\Gamma_s}\Psi_I^w v_s^w d\Gamma + \delta P_I\int_\Omega \Psi_{I,i}^w\frac{k_w}{\mu_w}\rho_w g_i d\Omega$$

Temporal Discretization

In time domain, the displacement is discretized by central difference scheme

$$d_{iI}^{n+1}=d_{iI}^n+\Delta t v_{iI}^n+0.5\Delta t^2 a_{iI}^n \quad (58)$$

$$v_{iI}^{n+1}=v_{iI}^n+0.5\Delta t\left(\mathrm{a}_{iI}^n+\mathrm{a}_{iI}^{n+1}\right) \quad (59)$$

Where Δt is time step size. The approach explicitly yields d_{iI}^{n+1} at the beginning of time step $n+1$. The predicted velocity is defined as

$$\hat{v}_{iI}^{n+1}=v_{iI}^n+0.5\Delta t a_{iI}^n \quad (60)$$

Pore water pressure is temporally discretized by forward Euler method and can be evaluated at the beginning of time step $n+1$ as

$$P_I^{n+1}=P_I^n+\Delta t\dot{P}_I^n \quad (61)$$

Rewriting equations (56) and (57) into matrix forms

$$\mathbf{M}\mathbf{a}^{n+1}+\mathbf{G}\mathbf{v}^{n+1}=\mathbf{F}^{\mathrm{ext}}-\mathbf{F}^{\mathrm{int}} \quad (62)$$

Citation: Siriaksorn T and Chi S. Multi-field Semi-Lagrangian Reproducing Kernel Particle Method for Landslide Simulation. SM J Biomed Eng. 2017; 3(2): 1014s.

Page 5/10

$$\mathbf{S}\dot{\mathbf{P}}^{n+1} = \tilde{\mathbf{F}}^{\text{ext}} - \tilde{\mathbf{F}}^{\text{int}} \tag{63}$$

$$
\text{with} \quad
\left.
\begin{aligned}
M_{IJ} &= \int_\Omega \Psi_I \rho \Psi_J d\Omega \\
G_{IJ} &= \int_\Omega \Psi_I \rho \overline{\Psi}_J d\Omega \\
F_{iI}^{\text{ext}} &= \int_{\Gamma_h} \Psi_I h_i d\Gamma \\
F_{iI}^{\text{int}} &= \int_\Omega \Psi_{I,j} \overline{\sigma}_{ij}^h d\Omega - \int_\Omega \Psi_{I,j} \alpha \Psi_J^w \delta_{ij} d\Omega P_J^{n+1} - \int_\Omega \Psi_I \rho g_i d\Omega \\
S_{IJ} &= \int_\Omega \Psi_I^w \frac{\Psi_J^w}{M} d\Omega \\
\tilde{F}_I^{\text{ext}} &= \int_{\Gamma_s} \Psi_I^w v_s^w d\Gamma \\
\tilde{F}_I^{\text{int}} &= \int_\Omega \Psi_I^w \alpha \Psi_{J,i} d\Omega v_{iJ}^{n+1} + \int_\Omega \Psi_{I,i}^w \frac{k_w}{\mu_w} \Psi_{J,i}^w d\Omega P_J^{n+1} - \int_\Omega \Psi_{I,i}^w \frac{k_w}{\mu_w} \rho_w g_i d\Omega
\end{aligned}
\right\} \tag{64}
$$

then applying temporal discretization from equations (58) - (61) by including mass proportional damping C, the fully discrete equations read

$$(\mathbf{M} + 0.5\Delta t(\mathbf{C}+\mathbf{G}))\mathbf{a}^{n+1} = \mathbf{F}^{\text{ext}} - \mathbf{F}^{\text{int}} - (\mathbf{C}+\mathbf{G})\hat{\mathbf{v}}^{n+1} \tag{65}$$

$$\mathbf{S}\dot{\mathbf{P}}^{n+1} = \tilde{\mathbf{F}}^{\text{ext}} - \tilde{\mathbf{F}}^{\text{int}} \tag{66}$$

The effect of convection matrix G on the accuracy of the solution is negligible [53]. The lumped mass scheme by the method of row summation is employed for M and S to acquire diagonal matrices. This can avoid solving system of equations and improve computational efficiency. In this paper, 5% mass proportional damping is used for C.

At each time step, a_{iI}^{n+1} is solved from equation (65), then v_{iI}^{n+1} is updated by equations (59) and (60), and substituted into equation (66) to determine $\dot{P}_I^{n+1}$.

Numerical Examples

Single-Field Semi-Lagrangian RKPM for Slope Stability Analysis

The semi-Lagrangian RKPM for landslide simulation is verified by comparing its result with the result from FEM [61]. In [61], under finite element framework, the Drucker-Prager parameter related to cohesion is reduced until the slope (Figure 4) is unstable according to the slip circle analysis. In this study, the critical value of cohesion from [61] is adopted (Table 1) to compare the slip surface when slope is unstable. The damage model incorporated in the framework is used as a means to identify the slip surface. Domain integration is carried out by MSNNI with number of subdomains Ns_I equal to 2 and stabilization parameter equal to 0.5 for each nodal representative domain. Natural and frictional kernel contact algorithms with a level set are employed to represent contacts between particles. The problem is discretized by 25,588 nodes.
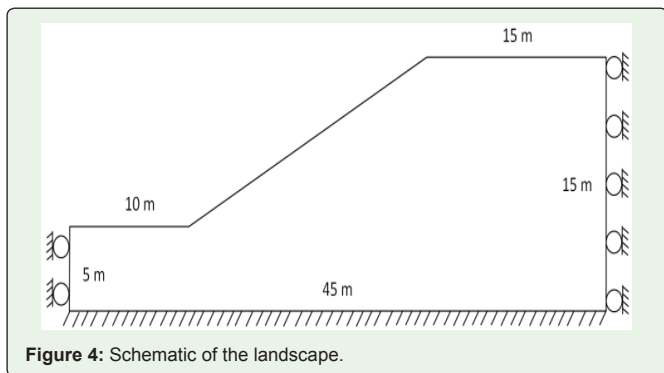

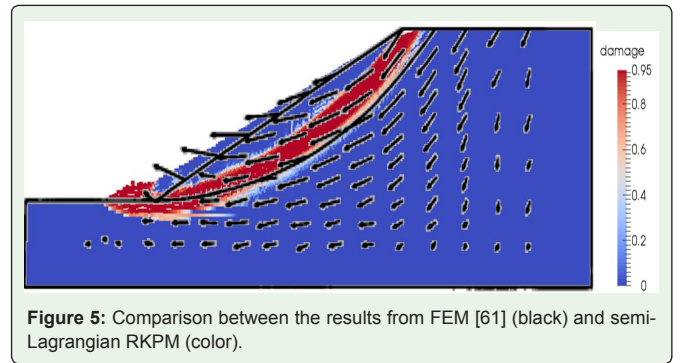**Figure 4:** Schematic of the landscape.

Figure 5: Comparison between the results from FEM [61] (black) and semi-Lagrangian RKPM (color).

The results from FEM [61] and this study are shown in Figure 5. The slip surface and displacement contour of the result from FEM [61] is illustrated by black solid lines and arrows, while the result from semi-Lagrangian RKPM is shown in color. From Figure 5, the semi-Lagrangian RKPM yields similar location of slip surface compared with FEM. The result verifies that the semi-Lagrangian RKPM is capable of effectively analyzing the slope stability.

One-Dimensional Consolidation

A 1-D consolidation problem subjected to a step load (Figure 6a) is analyzed to verify the performance of two-field semi-Lagrangian RKPM with MSNNI for saturated porous media. Stabilization parameter of 0.5 with 2 subdomains for each nodal representative domain is used. The specifications of the problem are shown in Table 2. The problem is discretized by 183 nodes (Figure 6b). Linear
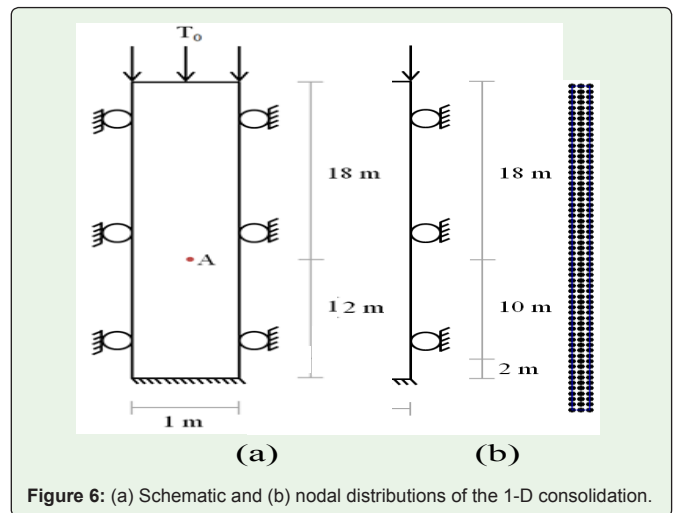

Figure 6: (a) Schematic and (b) nodal distributions of the 1-D consolidation.

Table 1: Material properties of the landscape.

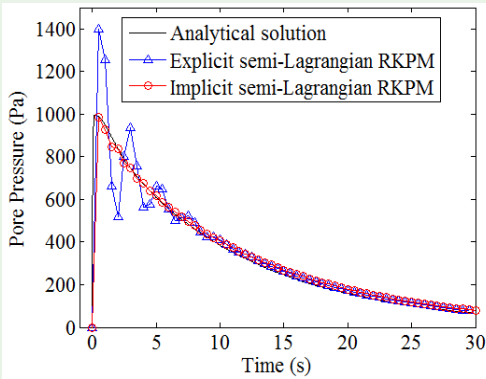|	
Young's Modulus (Pa) , E	2×10^8
Poisson's Ratio, V	0.25
Cohesion (Pa), C	2000
Friction Angle (°), ϕ	20
Damage Parameter: Initiation, C_2	0.05
Damage Parameter: Critical, C_1	1
Density (kg/m³), ρ	2039

Figure 7: Comparison of the results from semi-Lagrangian RKPM and the analytical solution at point A.

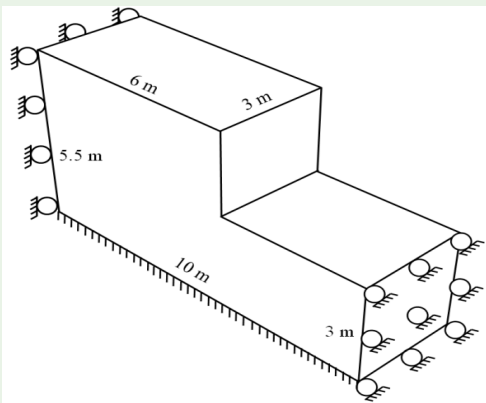

Figure 8: Schematic of the vertical-cut slope.

Table 2: Specification of the 1-D consolidation problem.

Young's Modulus (Pa), E	3×10^7
Poisson's Ratio, ν	0.2
Density (kg/m³), ρ	1700
Biot Coefficient, α	1
Biot Compressibility Modulus (Pa), M	3.33×10^8
Permeability $\left(\dfrac{\text{m}^2}{\text{Pa} \cdot \text{s}}\right)$, $\dfrac{k_w}{\mu_w}$	1.02×10^{-6}
Load (Pa), T_0	$1000 \sin\left(0.5\pi t/t_f\right)$ (Full load at $t = t_f = 0.1$ s)

elasticity is used to represent material behavior. The bottom of the problem is impervious while water can flow out freely on the top boundary ($P=0$). The pore pressure at the point of interest A (Figure 6a), is evaluated at the time from 0 to 30 seconds. The results from this study are compared with the analytical solution [43]. From Figure 7, the result from semi-Lagrangian RKPM using explicit temporal discretization exhibits oscillations at the beginning; however, after the oscillations taper off, the result is in good agreement with the analytical solution. Note that the oscillations at the beginning are from the use of explicit temporal discretization, which can be alleviated by using implicit temporal discretization with numerical damping (Newmark algorithm with β=0.3025 and γ=0.6) as discussed in [43] and as shown in Figure 7.

Two-Field Semi-Lagrangian RKPM for Landslide Simulation

To demonstrate the performance of semi-Lagrangian RKPM, the slide of a vertical-cut slope (Figure 8) is simulated. Semi-Lagrangian RKPM with MSNNI for saturated porous media is employed. The stabilization parameter and number of subdomains are the same as previous problems. The behaviors of solid phase of porous media
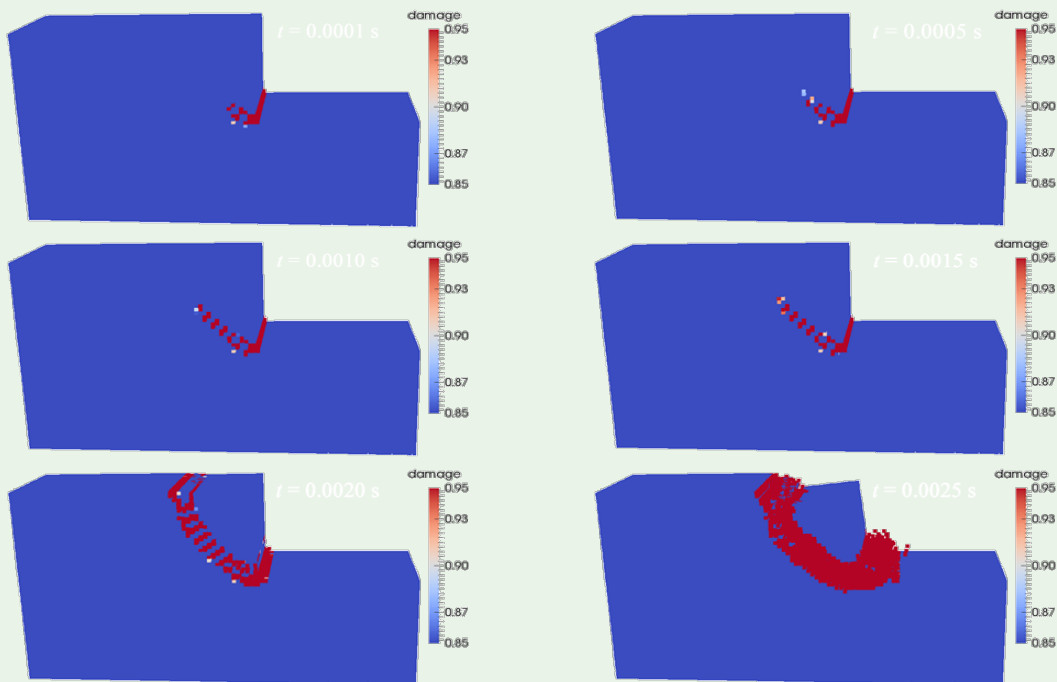

Figure 9: Two-field semi-Lagrangian RKPM landslide simulation of a vertical-cut slope.
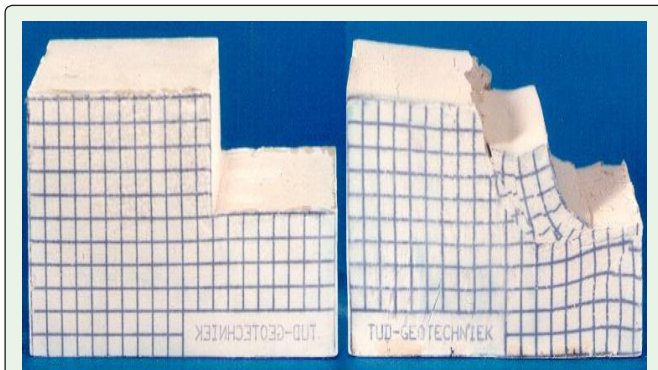
Figure 10: Experimental result from a centrifuge test of a vertical-cut slope (grid size is 5 mm) made by soft clay with 150 times of gravitational acceleration [62].

Table 3: Material parameters of the vertical-cut slope.

Young's Modulus (Pa), E	2.2×10^7
Poisson's Ratio, ν	0.2
Density (kg/m³), ρ	2900
Biot Coefficient, α	1
Biot Compressibility Modulus (Pa), M	3.33×10^8
Permeability $\left(\frac{m^2}{Pa \cdot s}\right)$, $\frac{k_w}{\mu_w}$	1.0×10^{-6}
Cohesion (Pa), c	5×10^4
Friction Angle (°), ϕ	15
Damage Parameter: Initiation, c_2	0.01
Damage Parameter: Critical, c_1	0.05

are represented by Drucker-Prager with damage models. Material parameters are shown in Table 3. The problem is discretized by 144,336 nodes. The bottom, left, and rightmost boundaries are impervious. The same contact algorithms as in the first problem are adopted.

The result shown in Figure 9 is validated by the experimental result of a soft clay sample from a centrifuge test with 150 times of the gravitational acceleration (Figure 10) [62]. From Figure 9 and Figure 10, the simulation from semi-Lagrangian RKPM has a similar failure pattern and deposition as in the experimental result from the centrifuge test. This problem demonstrates that the two-field semi-Lagrangian RKPM can determine accurate slip surface and predict landslide propagation.

Conclusions

This paper presents a displacement-pressure (u-p) semi-Lagrangian RKPM for modeling landslide activities. The method is developed based on the Galerkin formulation and, therefore, the constitutive models originally developed for FEMs can be directly incorporated. In addition, the semi-Lagrangian RK approximation is constructed purely based on a set of points in the deformation configuration; consequently, the method is capable of handling extreme deformation and material separation without encountering mesh related issues. The method offers a consistent modeling platform to analyze the whole spectrum of landslide processes as opposed to the combined methods, such as coupled FEM-DEM and coupled FEM-SPH, in which FEM is used for the pre-failure stage

and DEM or SPH for the post-failure or propagation stage of a landslide event. Although the construction of the semi-Lagrangian shape functions requires more computational effort, the fulfillment of consistency condition of the approximation ensures better solution accuracy. Furthermore, with the employment of the stabilized nodal integrations (SNNI and MSNNI) in the Galerkin formulation, the method takes advantage of using low order integration schemes while suppressing the instability due to spurious low energy modes.

The saturated multiphase porous model following the Biot theory is formulated in the u-p semi-Lagrangian RKPM, where the solid phase of porous media is modeled by the Drucker-Prager and damage models, to properly represent geomaterial behaviors. The explicit central difference time integration is adopted for dynamics analyses. The temporal stability of the central difference scheme in the u-p RKPM formulation will be the ongoing study. The results obtained from the present method are verified against analytical solutions and FEM results, which demonstrates that the method effectively determines the slip surface and pore water pressure. It is worthwhile to note that despite adopting an equal-order approximation scheme for the saturated u-p formulation, no significant pressure oscillation has been observed in the numerical study. The proposed method is validated with experimental results. The slip surface, failure pattern, as well as deposits in the simulation qualitatively agree with experimental data.

References

1. Close U, McCormick E. Where the Mountains Walked. National Geographic Magazine. 1922; 41: 445-472.

2. Feng X, Guo A. Earthquake landslides in China. In Proceedings, 4th International Conference and Field Workshop on Landslides. 1985; pp. 339-346.

3. Kaliser BN. Geologic hazards of 1983-Survey notes. Utah Geol & Min Surv. Salt Lake City. 1983; pp. 3-8.

4. University of Utah. Flooding and landslides in Utah: an economic impact analysis. Salt Lake City: University of Utah Bureau of Economic and Business Res., Utah Department of Community and Economic Development, and Utah Office of Planning and Budget. 1984; 123 p.

5. Cuomo S, Prime N, Iannone A, Dufour F, Cascini L, Darve F. Large deformation FEMLIP drained analysis of a vertical cut. Acta Geotechnica. 2013; 8: 125-136.

6. Spencer E. A Method of Analysis of the Stability of Embankments Assuming Parallel Inter-Slice Forces. Geotechnique. 1967; 17: 11-26.

7. Fellenius W. Calculation of the stability of earth dams. In Transactions of the 2nd congress on large dams, Washington, DC. 1936; 4: 445-463.

8. Fellenius W. Erdstatische Berechnungen, rev. ed. W. Ernst u. Sons, Berlin, 1927.

9. Taylor DW. Fundamentals of Soil Mechanics. Soil Sci. 1948; 66: 161.

10. N. Janbu. Slope stability computations: In Embankment-dam Engineering. Textbook. Eds. Hirschfeld RC and Poulos SJ. John Wiley and Sons Inc., Pub., NY, 1973, 40P. Int J Rock Mech Min. 1975; 12: 67.

11. Sarma SK. Stability analysis of embankments and slopes. Geotechnique. 1973; 23: 423-433.

12. Morgenstern NR, Price VE. The Analysis of the Stability of General Slip Surfaces. Geotechnique. 1965; 15: 79-93.

13. Bishop AW. The use of the Slip Circle in the Stability Analysis of Slopes. Geotechnique. 1955; 5: 7-17.

14. Cho SE, Lee SR. Instability of unsaturated soil slopes due to infiltration. Computers and Geotechnics. 2001; 28: 185-208.

Citation: Siriaksorn T and Chi S. Multi-field Semi-Lagrangian Reproducing Kernel Particle Method for Landslide Simulation. SM J Biomed Eng. 2017; 3(2): 1014s.

Page 8/10

15. Borja RI, White JA. Continuum deformation and stability analyses of a steep hillside slope under rainfall infiltration. Acta Geotechnica. 2010; 5: 1-14.

16. Conte E, Donato A, Troncone A. A finite element approach for the analysis of active slow-moving landslides. Landslides. 2014; 11: 723-731.

17. Lucy LB. A numerical approach to the testing of the fission hypothesis. Astronomical Journal. 1977; 82: 1013-1024.

18. Gingold RA, Monaghan JJ. Smoothed particle hydrodynamics: theory and application to non-spherical stars. Monthly Notices of the Royal Astronomical Society. 1977; 181: 375-389.

19. Randles PW, Libersky LD. Smoothed Particle Hydrodynamics: Some recent improvements and applications. Comput Method Appl M. 1996; 139: 375-408.

20. Monaghan JJ. SPH without a Tensile Instability. J Comput Phys. 2000; 159: 290-311.

21. Gray JP, Monaghan JJ, Swift RP. SPH elastic dynamics. Comput Method Appl M. 2001; 190: 6641-6662.

22. Pastor M, Haddad B, Sorbino G, Cuomo S, Drempetic V. A depth-integrated, coupled SPH model for flow-like landslides and related phenomena. Int J Numer Anal Met. 2009; 33: 143-172.

23. Hungr O, McDougall S. Two numerical models for landslide dynamic analysis. Comput Geosci. 2009; 35: 978-992.

24. McDougall S, Hungr O. A model for the analysis of rapid landslide motion across three-dimensional terrain. Can Geotech J. 2004; 41: 1084-1097.

25. Bui HH, Fukagawa R, Sako K, Ohno S. Lagrangian meshfree particles method (SPH) for large deformation and failure flows of geomaterial using elastic-plastic soil constitutive model. Int J Numer Anal Met. 2008; 32: 1537-1570.

26. Ataie-Ashtiani B, Shobeyri G. Numerical simulation of landslide impulsive waves by incompressible smoothed particle hydrodynamics. Int J Numer Meth Fl. 2008; 56: 209-232.

27. Rodriguez-Paz MX, Bonet J. A corrected smooth particle hydrodynamics method for the simulation of debris flows. Numer Meth Part D E. 2004; 20: 140-163.

28. Cundall PA, Strack ODL. A discrete numerical model for granular assemblies. Geotechnique. 1979; 29: 47-65.

29. Campbell CS, Cleary PW, Hopkins M. Large-scale landslide simulations: Global deformation, velocities and basal friction. J Geophys Res-Sol Ea. 1995; 100: 8267-8283, 1995.

30. Tang CL, Hu JC, Lin ML, Angelier J, Lu CY, Chan YC, et al. The Tsaoling landslide triggered by the Chi-Chi earthquake, Taiwan: Insights from a discrete element simulation. Eng Geol. 2009; 106: 1-19.

31. Cleary PW, Campbell CS. Self-lubrication for Long Runout Landslides: Examination by computer simulation. J Geophys Res-Sol Ea. 1993; 98: 21911-21924.

32. Cleary PW. Large scale industrial DEM modeling. Eng Computation. 2004; 21: 169-204.

33. Munjiza A, Owen DRJ, Bicanic N. A combined finite-discrete element method in transient dynamics of fracturing solids. Eng Computation. 1995; 12: 145-174.

34. Eberhardt E, Stead D, Coggan JS. Numerical analysis of initiation and progressive failure in natural rock slopes-the 1991 Randa rockslide. Int J Rock Mech Min. 2004; 41: 69-87.

35. Stead D, Eberhardt E, Coggan JS. Developments in the characterization of complex rock slope deformation and failure using numerical modelling techniques. Eng Geol. 2006; 83: 217-235.

36. Liu WK, Jun S, Zhang YF. Reproducing kernel particle methods. Int J Numer Meth Fl. 1995; 20: 1081-1106.

37. Chen JS, Pan C, Wu CT, Liu WK. Reproducing kernel Particle Methods for large deformation analysis of non-linear structures. Comput Method Appl M. 1996; 139: 195-227.

38. Guan PC, Chen JS, Wu Y, Teng H, Gaidos J, Hofstetter K, et al. Semi-Lagrangian reproducing kernel formulation and application to modeling earth moving operations. Mech Mater. 2009; 41: 670-683.

39. Guan PC, Chi SW, Chen JS, Slawson TR, Roth MJ. Semi-Lagrangian reproducing kernel particle method for fragment-impact problems. Int J Impact Eng. 2011; 38: 1033-1047.

40. Li S, Qian D, Liu WK, Belytschko T. A meshfree contact-detection algorithm. Comput Method Appl M. 2001; 190: 3271-3292.

41. Chi SW, Lee CH, Chen JS, Guan PC. A level set enhanced natural kernel contact algorithm for impact and penetration modeling. Int J Numer Meth Eng. 2014; 102: 839-866.

42. Biot MA. General Theory of Three-Dimensional Consolidation. J Appl Phys. 1941; 12: 155-164.

43. Zienkiewicz OC, Shiomi T. Dynamic behaviour of saturated porous media; The generalized Biot formulation and its numerical solution. Int J Numer Anal Met. 1984; 8: 71-96.

44. Zienkiewicz OC, Chan AHC, Pastor M, Schrefler BA, Shiomi T. Computational Geomechanics with Special Reference to Earthquake Engineering. Wiley Chichester, 1999.

45. Ju JW. On energy-based coupled elastoplastic damage theories: Constitutive modeling and computational aspects. Int J Solids Struct. 1989; 25: 803-833.

46. Simo JC, Ju JW. Strain-and stress-based continuum damage models-I. Formulation. Int J Solids Struct. 1987; 23: 821-840.

47. Simo JC, Ju JW. Strain-and stress-based continuum damage models-II. Computational aspects. Int J Solids Struct. 1987; 23: 841-869.

48. Hughes TJR, Winget J. Finite rotation effects in numerical integration of rate constitutive equations arising in large-deformation analysis. Int J Numer Meth Eng. 1980; 15: 1862-1867.

49. Bonet J, Kulasegaram S. Correction and stabilization of smooth particle hydrodynamics methods with applications in metal forming simulations. Int J Numer Meth Eng. 2000; 47: 1189-1214.

50. Beissel S, Belytschko T. Nodal integration of the element-free Galerkin method. Comput Method Appl M. 1996; 139: 49-74.

51. Chen JS, Wu CT, Yoon S, You Y. A stabilized conforming nodal integration for Galerkin mesh-free methods. Int J Numer Meth Eng. 2001; 50: 435-466.

52. Chen JS, Yoon S, Wu CT. Non-linear version of stabilized conforming nodal integration for Galerkin mesh-free methods. Int J Numer Meth Eng. 2002; 53: 2587-2615.

53. Wu Y. A Stabilized Semi-Lagrangian Galerkin Meshfree Formulation for Extremely Large Deformation Analysis. Ph.D. Thesis, UCLA, 2005.

54. Chen JS, Hu W, Puso MA, Wu Y, Zhang X. Strain Smoothing for Stabilization and Regularization of Galerkin Meshfree Methods. In Meshfree Methods for Partial Differential Equations III. 2007; 57: 57-75.

55. Puso MA, Chen JS, Zywicz E, Elmer W. Meshfree and finite element nodal integration methods. Int J Numer Meth Eng. 2008; 74: 416-446.

56. Chen JS, Hillman M, Rüter M. An arbitrary order variationally consistent integration for Galerkin meshfree methods. Int J Numer Meth Eng. 2013; 95: 387-418.

57. Lancaster P, Salkauskas K. Surfaces generated by moving least squares methods. Math Comput. 1981; 37: 141-158.

58. Ladyzhenskaya OA. The Mathematical Theory of Viscous Incompressible Flow. vol. 76. Gordon and Breach New York, 1969.

59. Babuška I. The finite element method with Lagrangian multipliers. Numerische Mathematik. 1973; 20: 179-192.

60. Brezzi F. On the existence, uniqueness and approximation of saddle-point problems arising from lagrangian multipliers. Revue française d'automatique, informatique, recherche opérationnelle. Analyse numérique, 1974; 8: 129-151.

61. Zienkiewicz OC, Humpheson C, Lewis RW. Associated and non-associated visco-plasticity and plasticity in soil mechanics. Geotechnique. 1975; 25: 671-689.

62. Allersma HG. Physical modelling of large granular systems in a centrifuge. In Symposium on Traffic and Granular Flow (TFG03), Delft, 2004.